

Adsorption of Charge-Bidisperse Mixtures of Colloidal Particles

Jeffrey J. Gray[†] and Roger T. Bonnecaze*

Department of Chemical Engineering, The University of Texas at Austin,
Austin, Texas 78712-1062

Received September 8, 2000. In Final Form: May 21, 2001

Careful control of the microstructure of an adsorbed monolayer of colloidal particles is important for creating nanostructured devices through self-assembly processes, and the structural and functional complexity of self-assembled particulate monolayers increases with the number of components in the system. Here, we perform simulations of the adsorption of binary mixtures of Brownian, colloidal particles to explore and identify combinations of parameters that produce technologically interesting surface structures. The system contains two types of particles of identical radii but differing surface potentials. In one scheme, Brownian dynamics simulations begin with an evenly distributed mixture above a charged planar surface, and the particles adsorb to the surface until the system achieves a steady state. In the second scheme, two different single-component suspensions are exposed to the substrate sequentially. Volume fractions in the bulk control relative surface coverages, and the observed structures include isolated, high-potential particles and chains and clusters of low-potential particles. Substitutionally disordered lattices form for ratios of particle potential ranging from about 1.5 to 4, depending on parameters: ordered lattices are more stable to bidispersity at higher wall potentials and higher particle potentials. Terminal fractional bidispersities based on equivalent hard disk (EHD) radii vary from 3.6 to 10%. In sequential adsorption, small amounts of the second component adsorb only for parameter combinations with minimal repulsions from preadsorbed particles and sufficient attraction to the surface, since colloidal adsorption is a kinetically frustrated process. High-potential particles added to a monolayer of low-potential particles create isolated dots, and in reverse, low-potential particles dope lattices of high-potential particles. The results of the simulations are discussed in the light of lattice models and EHD models.

Introduction

Adsorption of colloidal particles is a potentially useful “bottom-up” assembly technique for the manufacture of materials with surfaces with designed small-scale features. Applications from nanowires¹ to photonic devices² have been proposed as candidates for assembly from particles in suspension. Additional structural and functional complexity can be introduced by including multiple types of particles. For example, a bifunctional catalyst recently developed for purifying air in medical facilities operates by separating electron-hole pairs on different types of colloidal particles for photocatalytic redox chemistry.³ In a previous paper,⁴ we developed a simulation tool to study kinetics and structure formation in the adsorption of colloidal particles. Here, we extend the technique to ζ -potential bidisperse mixtures of particles and explore the possibilities for creating interesting surface structures with these mixtures.

The simplest theoretical studies of adsorption of bidisperse mixtures are those carried out on a regular lattice. On a lattice, the bidisperse adsorption problem can be mapped to the three-state Potts (generalized Ising) model.⁵ Schick has reviewed order/disorder transitions in systems with various two-dimensional lattice geometries (e.g., skew, rectangular, centered rectangular), including clas-

sifying the order of the transitions and deriving critical exponents.⁶ Depending on the energy of the ground states and the coupling parameters between neighboring sites, ordered and disordered phases are possible, including the $\sqrt{2} \times \sqrt{2}$ checkerboard pattern on a square lattice and the $\sqrt{3} \times \sqrt{3}$ or AB₂ phase on a triangular lattice. Rikvold and co-workers have applied lattice-gas models to multicomponent colloidal adsorption on a triangular lattice.^{7–10} They used two-dimensional transfer-matrix techniques, Monte Carlo simulations, and finite-size scaling analyses to capture equilibrium states considering energetic interactions between the particles, their neighbors, and the substrate. They produced phase diagrams and found that interactions between species can create cooperative behavior such as poisoned and enhanced adsorption.

Although lattice systems can be revealing, their applicability is limited to cases where adsorption can only occur in discrete places. This is appropriate for atomic adsorption onto a crystal plane, but particles in the nanometer to micron range are significantly larger than atomic sites and will therefore interact in an off-lattice continuum fashion. The most complete study of the surface structures available to bidisperse mixtures of hard disks in two dimensions was performed by Likos and Henley.¹¹ They enumerated possible regular structures and their

* Corresponding author e-mail: rtb@che.utexas.edu.

[†] Present address: Department of Biochemistry, University of Washington, Seattle, WA 98195; e-mail: jjgray@u.washington.edu.

(1) Korgel, B. A.; Fitzmaurice, D. *Adv. Mater.* **1998**, *10*, 661–665.

(2) Yablonovitch, E. *J. Opt. Soc. Am. B* **1993**, *10*, 283–295.

(3) Sitkewitz, S. D. Ph.D. Thesis, The University of Texas at Austin, Austin, TX, 1999.

(4) Gray, J. J.; Bonnecaze, R. T. *J. Chem. Phys.* **2001**, *114*, 1366–1381.

(5) Wu, F. Y. *Rev. Mod. Phys.* **1982**, *54*, 235–268.

(6) Schick, M. *Prog. Surf. Sci.* **1981**, *11*, 245–292.

(7) Collins, J. B.; Rikvold, P. A.; Gawlinski, E. T. *Phys. Rev. B: Condens. Matter* **1988**, *38*, 6741–6750.

(8) Rikvold, P. A.; Collins, J. B.; Hansen, G. D.; Gunton, J. D. *Surf. Sci.* **1988**, *203*, 500–524.

(9) Collins, J. B.; Sacramento, P.; Rikvold, P. A.; Gunton, J. D. *Surf. Sci.* **1989**, *221*, 277–298.

(10) Rikvold, P. A.; Zhang, J.; Sung, Y.-E.; Wieckowski, A. *Electrochim. Acta* **1996**, *41*, 2175–2184.

(11) Likos, C. N.; Henley, C. L. *Philos. Mag. B* **1993**, *68*, 85–113.

symmetries for various ratios of particle sizes and densities. By minimizing the area per particle of the structures, they created a phase diagram of the equilibrium phases at zero temperature with no entropy of mixing. Segregated pure phases are the equilibrium structure for particle size ratios between 0.637 and unity, but as the size ratio decreases, the number of different ordered phases increases dramatically and becomes innumerable.

Similar studies performed on three-dimensional systems are worth noting. Cottin and Monson recently used cell models to determine solid–fluid equilibria for bidisperse hard spheres and Lennard–Jones particles.^{12–15} Earlier, Murray and Sanders¹⁶ and Eldridge et al.¹⁷ calculated the packing density of bidisperse hard spheres to delineate the size ratios that give rise to AB, AB₂, and AB₁₃ packings. These latter studies have been cited recently to explain experimentally constructed AB₂ monolayers of nanoparticles for size ratios of 0.58,¹⁸ even though two-dimensional calculations¹¹ do not predict AB₂ structures at this size ratio. Finally, three-dimensional Monte Carlo simulations on charge-bidisperse particles have located the solid–fluid transition point at a fractional standard deviation of 26% charge polydispersity, considerably higher than the size polydispersity limit of 11%.^{19,20}

Three-dimensional studies of the adsorption of mixtures are limited. González-Mozuelos et al.²¹ used density functional theory to self-consistently calculate equilibrium surface coverages and the density profiles as a function of distance from the surface for each component of the mixture. While the predicted structure in the bulk of the suspension is accurate, it is likely that the surface coverages are overpredicted, since particle repulsions frustrate the adsorption process before equilibrium is reached.⁴ Three-dimensional dynamic simulations of the adsorption of colloidal mixtures have not been performed.

Recently, we developed efficient parallel simulations for the adsorption of colloidal particles onto a surface.⁴ The simulations include mean-field boundary conditions at the (open) top of the simulation box and flux both into and out of the box to maintain a constant chemical potential as the particles adsorb onto the surface. Our simulations showed that the ζ -potential of the particles controls the coverage on the surface and that the ζ -potential of the wall can be used to make moderate changes in the coverage, which induce the monolayer to order into a regular triangular lattice. We demonstrated that the final surface coverage is not determined by equilibrium: adsorption ceases below the equilibrium coverage because repulsions between adsorbed particles and bulk particles prevent further adsorption. Thus, colloidal adsorption is a nonequilibrium process, and kinetic simulation is an effective means to capture system behavior and in particular to determine the monolayer structures that can be assembled from solution.

In this paper, we extend our colloidal adsorption simulations to mixtures that are bidisperse in particle

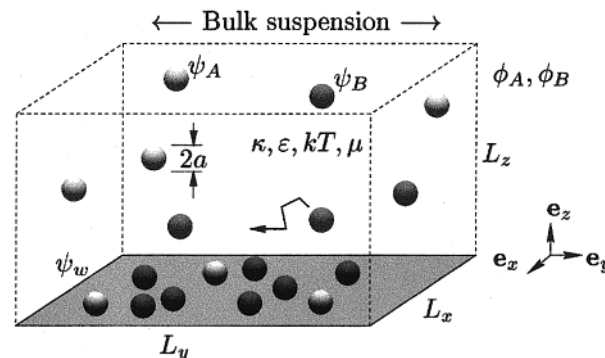


Figure 1. Diagram of the adsorption of binary mixtures of colloidal particles.

ζ -potential. We explore the effect of varying the relative volume fractions of the two components and of varying the ratio of particle potentials. We employ two adsorption schemes: first, adsorbing both types of particles simultaneously from a mixed suspension and, second, adsorbing from two single-component suspensions in a two-part process. We focus our studies on a search for interesting surface structures for self-assembled nanotechnological applications.

Formulation

Problem Statement. We model the bidisperse problem here analogously to the monodisperse case of ref 4. A semi-infinite suspension bounded by a wall at $z = -a$ contains particles of types A and B in volume fractions ϕ_A and ϕ_B , respectively (Figure 1). Both types of particles are spherical with radius a , but they differ in their surface properties: the ζ -potentials of A and B particles are ψ_A and ψ_B , respectively, with $\psi_A\psi_B > 0$ so that all particle–particle interactions are repulsive. The suspending fluid has a viscosity μ , an electrostatic permittivity ϵ , and a Debye inverse screening length κ , as determined by the ionic strength of the fluid. The density difference between the particles and the fluid is assumed to be negligible. Thermal energy in the system is characterized by kT , where k is Boltzmann's constant and T is temperature. Particles are assumed to be Brownian, so we consider particles with sizes ranging from 20 nm to 1 μ m.

The electrostatic interactions among the particles are assumed to follow a pairwise Yukawa potential. Because different particles have different ζ -potentials, interaction potentials depend on the particle species:

$$V_{iw} = 4\pi\epsilon a\psi_i\psi_w e^{-\kappa z} \quad (1)$$

$$V_{ij} = 4\pi\epsilon a^2\psi_i\psi_j e^{2\kappa a} \frac{e^{-\kappa r_{ij}}}{r_{ij}} \quad (2)$$

where V_{iw} is the potential between particle i and the wall; V_{ij} is the potential between particles i and j ; ψ_i , ψ_j , and ψ_w are the surface ζ -potentials on particles i and j and the wall; and r_{ij} is the distance between the centers of particles i and j . The forces are then

$$\mathbf{F}_{iw} = 4\pi\epsilon a\psi_i\psi_w \kappa e^{-\kappa z} \mathbf{e}_z \quad (3)$$

$$\mathbf{F}_{ij} = 4\pi\epsilon a^2\psi_i\psi_j e^{2\kappa a} \left(\frac{1}{r_{ij}} + \kappa \right) \frac{1}{r_{ij}} e^{-\kappa r_{ij}} \mathbf{e}_{r_{ij}} \quad (4)$$

where \mathbf{F}_{iw} is the force between particle i and the wall; \mathbf{F}_{ij} is the force between particles i and j ; \mathbf{e}_z is the unit vector

- (12) Cottin, X.; Monson, P. A. *J. Chem. Phys.* **1993**, *99*, 8914–8921.
- (13) Cottin, X.; Monson, P. A. *J. Chem. Phys.* **1995**, *102*, 3354–3360.
- (14) Cottin, X.; Monson, P. A. *J. Chem. Phys.* **1996**, *105*, 10022.
- (15) Cottin, X.; Monson, P. A. *J. Chem. Phys.* **1997**, *107*, 6855–6858.
- (16) Murray, M. J.; Sanders, J. V. *Phys. Rev. A: At., Mol., Opt. Phys.* **1980**, *42*, 721–740.
- (17) Eldridge, M. D.; Madden, P. A.; Frenkel, D. *Nature* **1993**, *365*, 35–37.
- (18) Kiely, C. J.; Fink, J.; Brust, M.; Bethell, D.; Schiffrin, D. J. *Nature* **1998**, *396*, 444–446.
- (19) Tata, B. V. R.; Arora, A. K. *J. Phys.: Condens. Matter* **1991**, *3*, 7983–7993.
- (20) Tata, B. V. R.; Arora, A. K. *J. Phys.: Condens. Matter* **1992**, *4*, 7699–7708.
- (21) González-Mozuelos, P.; Medina-Noyola, M.; D'Aguanno, B.; Méndez-Alcaraz, J. M.; Klein, R. *J. Chem. Phys.* **1991**, *95*, 2006–2011.

in the z direction (normal to the adsorption surface); and $\mathbf{e}_{r_{ij}}$ is the unit vector along the direction of particle centers.

The motion of each particle in the suspension follows the Langevin equations for Stokesian particles:

$$\dot{\mathbf{x}}_i = \frac{\mathbf{D}_i}{kT}(\mathbf{F}_i^P + \mathbf{F}_i^B) \quad (5)$$

where $\dot{\mathbf{x}}_i$ is the velocity vector of particle i , \mathbf{D}_i is the diffusivity tensor of particle i , \mathbf{F}_i^P represents the deterministic forces acting on particle i , and \mathbf{F}_i^B represents the Brownian forces acting on particle i , with the hydrodynamic interactions between particles neglected in the diffusivity tensor. The Brownian force has moments $\langle \mathbf{F}_i^B(t) \rangle = 0$ and $\langle \mathbf{F}_i^B(0) \mathbf{F}_i^B(t) \rangle = 2\mathbf{D}_i^{-1}kT\delta(t)$, where $\delta(t)$ is the Dirac delta function.

Interparticle hydrodynamic interactions can reasonably be neglected because the volume fraction of particles is small. At $\phi_A + \phi_B = 0.01$, the average nearest-neighbor distance in the bulk is $8.4a$, and hydrodynamic coupling transmits less than 10% of transverse forces and less than 20% of normal forces to a nearest-neighbor particle (eq 6-2.10 in ref 22). On the surface, where particle concentration is higher, nearest-neighbor distances can be half of that in the bulk, and hydrodynamic coupling between particles can transmit 20–40% of forces. However, at the surface, lubrication interactions with the wall dominate the calculation of the mobility tensor. Therefore, we approximate the mobility as a function of only the gap z between each particle and the wall:

$$\mathbf{M}(z) = \frac{1}{6\pi\mu a}[\tilde{M}_\perp(z)\mathbf{e}_z\mathbf{e}_z + \tilde{M}_\parallel(z)(\mathbf{e}_x\mathbf{e}_x + \mathbf{e}_y\mathbf{e}_y)] \quad (6)$$

where $\tilde{M}_\perp(z)$ and $\tilde{M}_\parallel(z)$ range from 0 to 1 and are the corrections to the mobility in the presence of the wall for motion perpendicular and parallel to the wall. Formulas for $\tilde{M}_\perp(z)$ and $\tilde{M}_\parallel(z)$ are tabulated in Appendix A of ref 4.

As in ref 4, the particle radius (a), the thermal energy (kT), the fluid viscosity (μ), and the electrostatic permittivity (ϵ) are used to scale the parameters in the problem to create nondimensional variables denoted with hats:

$$\hat{\mathbf{x}} = \frac{\mathbf{x}}{a}, \hat{\kappa} = a\kappa, \hat{t} = \frac{kTt}{6\pi a^3\mu}, \hat{\mathbf{x}} = \frac{6\pi a^2\mu\dot{\mathbf{x}}}{kT},$$

$$\hat{\mathbf{F}} = \frac{a\mathbf{F}}{kT}, \hat{V} = \frac{V}{kT}, \Psi_i = \left(\frac{4\pi\epsilon a}{kT}\right)^{1/2}\psi_i,$$

$$\Psi_w = \left(\frac{4\pi\epsilon a}{kT}\right)^{1/2}\psi_w, \text{ and } \hat{\mathbf{D}} = \hat{\mathbf{M}} = \frac{6\pi\mu a\mathbf{D}}{kT} = 6\pi\mu a\mathbf{M}$$

The nondimensional system is solved computationally; in the remaining text, the nondimensional quantities are used, and the hat notation is dropped for convenience.

Computational Algorithm. The motion of a set of particles in a suspension is calculated within a box of dimensions $L_x \times L_y \times L_z$. The box is periodic in the x and y directions, and the wall is placed at $z = -a$ so that the particle centers have a minimum coordinate of 0. The top of the box represents a boundary with the bulk fluid. To accelerate computation in these exploratory studies, some simulations are performed with short boxes ($10 \leq L_z \leq 20$), simulating a diffusion boundary layer between the substrate and the bulk suspension at a constant, well-mixed volume fraction. For studies of adsorption from a

bidisperse suspension, particles are placed initially at random positions within the box so that the volume fractions match those of the bulk, ϕ_A and ϕ_B . In the case of sequential runs, a monodisperse simulation is performed, and then all particles that are not on the surface ($z > 1$) are removed. The simulation box is then repopulated with particles of the new type so that the volume fraction of the top portion of the box ($z > 5$) matches that of the second suspension. Particle motions are integrated using the midpoint algorithm as described by Grassia et al.²³ and detailed in ref 4.

Mean-Field Forces from the Bulk. Particles in the bulk of the suspension exert colloidal forces on the particles within the suspension box, and the magnitude of this force is determined with a mean-field approximation, here generalized for two (or more) components. The repulsive force on particle i in the simulation box from particles in the bulk of the suspension is

$$\mathbf{F}_i^{\text{MF}}(\mathbf{x}) = \int_{\Omega} \sum_{j=A,B} n_j(\mathbf{y}) \mathbf{F}_{ij}(\mathbf{y} - \mathbf{x}) d\mathbf{y} \quad (7)$$

$$= \int_{\Omega} \sum_{j=A,B} n_j g_{ij}(r) \mathbf{F}_{ij}(\mathbf{r}) d\mathbf{r} \quad (8)$$

$$= \mathbf{e}_z \pi \int_H \left(1 - \frac{h^2}{r^2}\right) \sum_{j=A,B} (n_j g_{ij}(r) \mathbf{F}_{ij}(r)) r^2 dr \quad (9)$$

where Ω is the volume of the bulk suspension above the simulation box, \mathbf{y} is a location in Ω , $n_j(\mathbf{y})$ is the expected number density of particles of type j at \mathbf{y} , and $\mathbf{F}_{ij}(\mathbf{y} - \mathbf{x})$ is the force imposed by a particle of type j at \mathbf{y} onto particle i located at \mathbf{x} within the simulation box. In the second line, \mathbf{r} is the vector $\mathbf{y} - \mathbf{x}$, $r = |\mathbf{r}|$, $g_{ij}(r)$ is the equilibrium pair distribution function for particles of type i and j , and $n_j = 3\phi_j/4\pi$ is the number density of particles of type j in the bulk. The pair distribution functions must correspond to the equilibrium state of the bidisperse suspension: they are the autocorrelation functions $g_{AA}(r)$ and $g_{BB}(r)$ and the cross-correlation function $g_{AB}(r) = g_{BA}(r)$, precalculated with a bidisperse, Metropolis-method Monte Carlo simulation.²⁴ Finally, $h = L_z - z$ is the distance between the particle center and the top of the simulation box, and H is the maximum of 2 and h . In practice, the integrals in eq 9 are pretabulated for rapid use during the simulation.

Grand Canonical Brownian Dynamics. The number of particles simulated fluctuates in time as particles enter and leave the simulation box. To capture these events, we follow the procedure developed in ref 4, with the following change. To generalize the boundary condition for two components, the potential due to particles above the simulation box, used for calculating new particle acceptance probabilities, must include interactions with both species:

$$V_i^{\text{MF}}(h) = \int_{\Omega} \sum_{j=A,B} n_j g_{ij}(r) V_{ij}(r) d\mathbf{r} \quad (10)$$

where the equilibrium pair distribution functions from a Monte Carlo simulation are again used.

Figure 2 shows the forces and potentials acting on particles of a bidisperse suspension for a typical set of parameters. In this case, the presence of the top of the box is "felt" by A particles at $h \leq 6$ and by B particles at $h \leq$

(22) Happel, J.; Brenner, H. *Low Reynolds Number Hydrodynamics, with Special Applications to Particulate Media*; Prentice Hall International Series in the Physical and Chemical Engineering Sciences; Prentice Hall: Englewood Cliffs, NJ, 1965.

(23) Grassia, P. S.; Hinch, E. J.; Nitsche, L. C. *J. Fluid Mech.* **1995**, *282*, 373–403.

(24) Allen, M. P.; Tildesley, D. J. *Computer Simulation of Liquids*; Oxford University Press: Oxford, 1987.

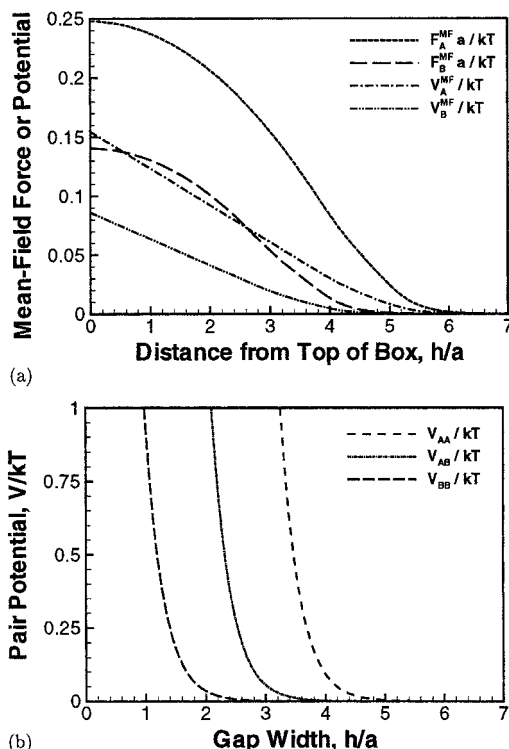


Figure 2. (a) Mean-field forces and potentials acting on particles near the top of the simulation box as determined by a Monte Carlo simulation and eqs 9 and 10. System parameters: $\kappa = 3$, $\phi_A = \phi_B = 0.005$, $\Psi_A = 300$, $\Psi_B = 7.5$. (b) Shown for reference are the interaction potentials between pairs of particles, where h represents the gap width between particles.

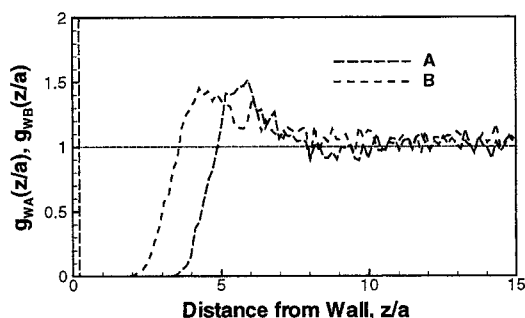


Figure 3. Typical density profile for a two-component mixture above a charged wall, normalized by the bulk volume fractions. System parameters: $\kappa = 3$, $\phi_A = \phi_B = 0.005$, $\Psi_A = 300$, $\Psi_B = 7.5$. Statistical data collected at time intervals of $\Delta t = 1$ during the period $2400 < t < 3160$.

4, distances slightly greater than the extent of the two-particle interaction potentials.

Figure 3 shows the resulting density profiles in a typical bidisperse system near the end of the adsorption process. The adsorbed layer is represented by the spike in the profile near $z/a = 0$. Repulsions between particles in the bulk and particles adsorbed on the surface create a depletion region free of particles: the more highly charged A particles are absent for $0 \leq z < 4$, and the lower potential B particles are absent for $0 \leq z < 2.5$. After the depletion region, both species show a density maximum near $1.5 \times$ their bulk volume fractions, representing the structure of the first layer of particles in the bulk. For $z > 10$, the densities of both species fluctuate around their bulk value, indicating that the chemical potential has been set as desired.

The simulation algorithm is programmed for parallel architecture machines, tracking neighbors of each particle

for faster computation of forces. Runs require 3–30 h of processing time using 2–4 nodes of a Cray T3E super-computer.

Monolayer Morphologies in Bidisperse Systems

Mixing Effects. Figure 4 shows the effects of mixing of two components as the ratio of ϕ_A/ϕ_B is varied, while holding total volume fraction constant at 0.01. The ζ -potential, or bidispersity, is $\lambda \equiv \Psi_A/\Psi_B = 40$, and $\Psi_A = 300$. At the low volume fractions of $\phi_A = 0.0005$, the high-potential A (white) particles create islands in the sea of low-potential (black) particles. Because of the increased repulsion from the A particles, there is a relatively large gap between the A particles and their neighbors. No A particles have neighbors of like type, and the isolation of the A particles could make them useful as quantum dots. As ϕ_A increases, the A particles on the surface no longer remain isolated from each other, and pairs and larger clusters of A particles exist with isolated particles. At $\phi_A = 0.0025$ and 0.005, clusters of A and B particles show local demixing, although the species do not phase separate completely. As ϕ_A increases toward 0.01, a regular triangular lattice structure begins to form (note, however, that at these conditions a monodisperse lattice of A (white) particles will not order completely), and the B particles create defects and bend the lines of particles.

Figure 5 shows the jamming limit surface coverage determined by extrapolating kinetic data to infinite time using a 2/3-power law ($\theta_\infty - \theta \sim t^{-2/3}$ as $t \rightarrow \infty$).²⁵ The fraction of each type of particle on the surface reflects that in the bulk, and the total coverage on the surface decreases smoothly from the coverage of a monodisperse lattice of B particles to one of A particles. For $\lambda = 4.2$, the partition behavior is close to ideal, but the $\lambda = 40$ case departs from linearity in the coverage vs volume fraction curves. Although the behavior is not particularly unusual, note that varying the volume fraction of one component in a mixture is significantly different from varying the volume fraction in a monodisperse system, where surface coverage is constant over orders of magnitude of ϕ .⁴ Thus, competitive adsorption, or mixing, provides an effective means for varying the coverage of a desired component on a surface.

Bidispersity in Disordered Systems. Figure 6 shows two typical surfaces with adsorbed particles and their corresponding radial pair distribution functions for small and large bidispersity in the ζ -potential for conditions where monodisperse systems do not order. For small bidispersity, $\lambda = 4.2$, the pair distribution functions for the A and B particles are slightly out of phase. The surface structure shows a well-mixed liquidlike configuration. The $\lambda = 40$ simulation also reveals a liquid-like morphology; however, it shows additional structuring. The B particles cluster together more tightly, and the A particles create additional open space around them. The pair distribution functions reflect this behavior: $g_{AA}(r)$ is noticeably displaced from $g_{BB}(r)$, revealing that the typical AA distance is almost as large as the BB distance between second-nearest neighbors.

We can compute dimensional time using the scalings from the end of the section titled Problem Statement. The characteristic time, t_c , equals $6\pi a^3 \mu / kT$. For 100 nm particles in water at room temperature, $t_c \approx 1.4$ s. For the systems in Figure 6a,c, where the final dimensionless times are 3000 and 3260, respectively, the dimensional times are 4000–4500 s or somewhat over 1 h. This

(25) Schaaf, P.; Johnner, A.; Talbot, J. *Phys. Rev. Lett.* **1991**, *66*, 1603–1605.

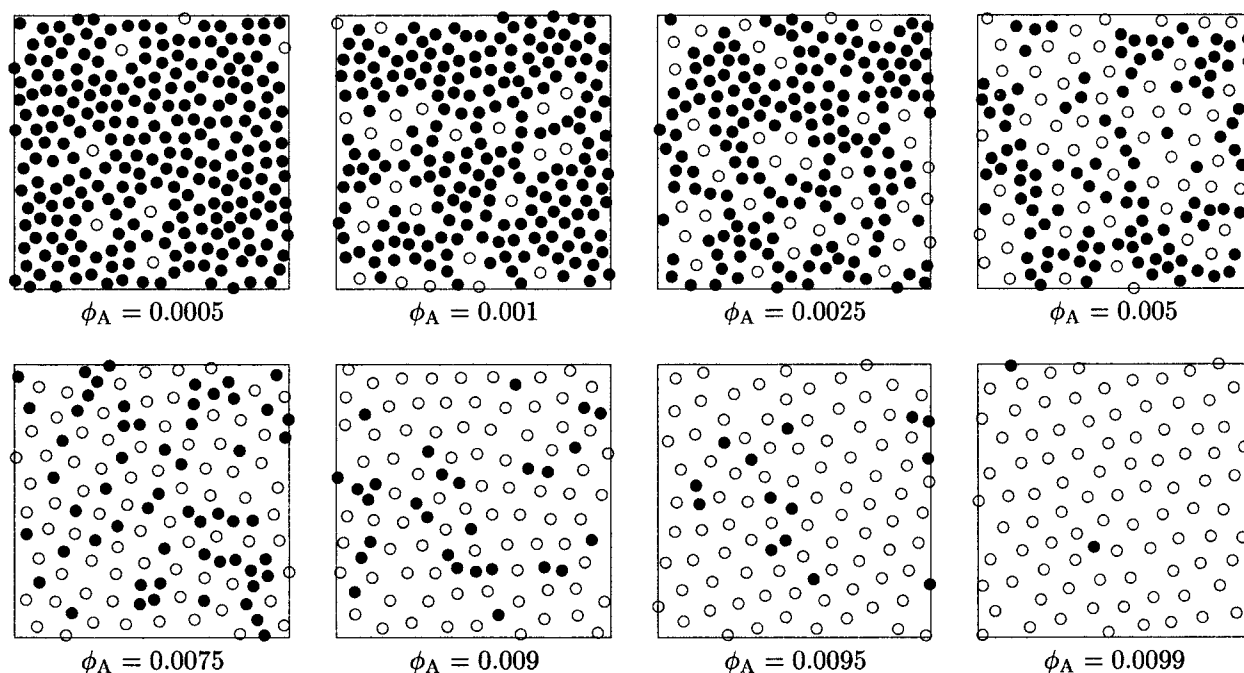


Figure 4. Surface structures showing the effects of mixing two components. The volume fractions of A and B are varied with the total volume fraction constant at 0.01. $\kappa = 3$, $\Psi_W = -27.3$, $\Psi_A = 300$, $\Psi_B = 7.5$ ($\lambda = 40$). Here and in subsequent figures, white and black particles are the high- and low-potential species, A and B, respectively.

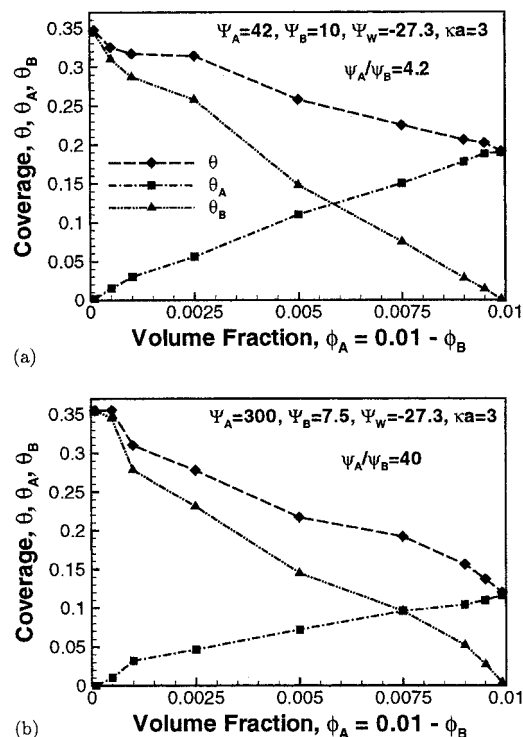


Figure 5. Jamming coverage of A and B particles as a function of bulk concentration of A. The total volume fraction, $\phi_A + \phi_B$, is constant at 0.01. (a) Small bidispersity, $\lambda = 4.2$ ($\Psi_A = 42$, $\Psi_B = 10$). (b) Large bidispersity, $\lambda = 40$ ($\Psi_A = 300$, $\Psi_B = 7.5$). For both data sets, $\Psi_W = -27.3$, and $\kappa = 3$. Jamming limits are determined by extrapolating kinetic data to infinite time using a $2/3$ -power law.²⁵

illustrates that colloidal systems are convenient for studying adsorption phenomena in real time.

Figure 7 demonstrates how the adsorption of mixed monolayers might be used to template patterns. After a bidisperse suspension is exposed to a surface and particles adsorb, one of the two components can be selectively

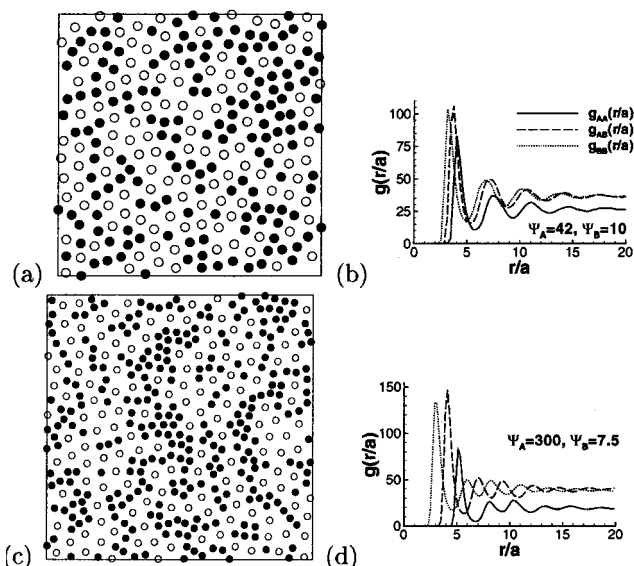


Figure 6. Typical surface structures (a, c) and corresponding radial distribution functions (b, d). (a, b) $\lambda \equiv \Psi_A/\Psi_B = 4.2$; (c, d) $\lambda = 40$. In both simulations, $\Psi_W = -27.3$, $\kappa = 3$, and $\phi_A = \phi_B = 0.005$. In panel a, $t = 3000$, $L_x = L_y = 60$, and $L_z = 50$; in panel c, $t = 3260$, $L_x = L_y = 80$, and $L_z = 10$. Surface pair distribution functions are normalized by the bulk volume fractions and the monolayer thickness of one particle diameter.

desorbed, leaving one remaining component in a surface structure that might not have been obtainable through single-component adsorption. The surface in Figure 7a has a coverage much less than that which would result from adsorption from a suspension containing only A particles. Figure 7b reveals percolating chains and clusters in arrangements unlike any seen in the monodisperse studies of ref 4.

Bidispersity-Induced Order/Disorder Transition. As shown in ref 4, large-magnitude wall potentials induce repulsive particles to adsorb onto a surface and spontaneously order into a hexagonal array. Monolayers order

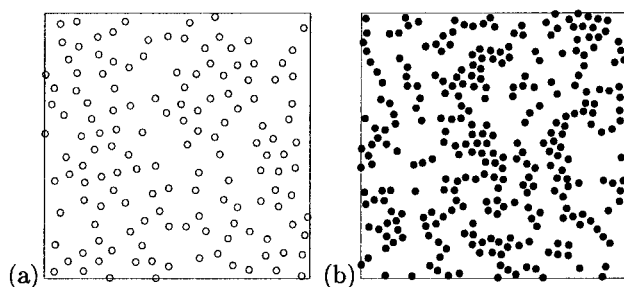


Figure 7. Templated structures formed by selective removal of one component from the system in Figure 6c. (a) A structure after removal of B. (b) B structure after removal of A.

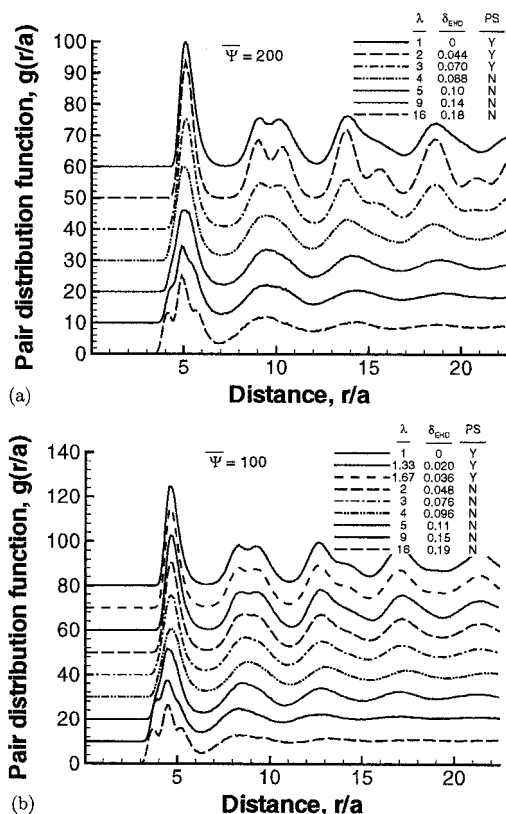


Figure 8. Pair distribution functions of adsorbed particles showing the breakup of order as bidispersity is introduced for $\kappa = 3$, $\Psi_w = -100$, and $\phi_A = \phi_B = 0.005$. (a) $\bar{\Psi} = \sqrt{\Psi_A \Psi_B} = 200$, (b) $\bar{\Psi} = 100$. In the legends, $\lambda = \Psi_A/\Psi_B$ is the ζ -potential bidispersity, δ_{EHD} is the fractional standard deviation of the EHD size bidispersity (defined in the text), and "PS" indicates the presence of peak-splitting in the second shell of neighbors.

because larger wall potentials attract a higher concentration of particles. At sufficiently dense monolayer packings, the repulsive particle interactions overcome the thermal energy present in the system and find the energetic minimum where particles are maximally separated in an ordered triangular lattice. Here, we choose conditions in the ordered regime and explore the breakup of order as the bidispersity in particle ζ -potentials increases.

To measure the overall order of the combined AB lattice, Figure 8 displays total pair correlation functions (including both particle species) for systems with $\phi_A = \phi_B = 0.005$, short-range interactions ($\kappa = 3$), and $\Psi_w = -100$. In each series, the geometric mean of the particle potentials ($\bar{\Psi} = \sqrt{\Psi_A \Psi_B}$) is constant, and the bidispersity ($\lambda = \Psi_A/\Psi_B$) varies. We test the degree of order in the system by observing the presence of "peak-splitting." The second broad peak in the pair distribution function splits into

two peaks when the second- and third-nearest neighbors on a triangular lattice (both in the second shell) are sufficiently distinct. In monodisperse systems, peak-splitting occurs in ordered systems but not in disordered systems, and in random sequential adsorption studies of hard disks, the rise of peak-splitting corresponds to the boundary between the liquid and the hexatic phases.^{4,26} For $\bar{\Psi} = 200$ (Figure 8a), systems with bidispersity of $\lambda \leq 3$ exhibit peak-splitting, and those with $\lambda \geq 4$ do not. For a lower mean particle potential of $\bar{\Psi} = 100$ (Figure 8b), the boundary occurs at a lower bidispersity: peak-splitting is observed for $\lambda \leq 1.67$, and peaks do not split for $\lambda \geq 2$. As in monodisperse systems,⁴ larger particle potentials stabilize order.

Figure 9a shows the surface morphologies corresponding to the pair distribution functions in Figure 8a. For $\lambda = 2$, the two types of particles are randomly interspersed in a regular lattice. This morphology has been referred to as "substitutionally disordered". At $\lambda = 3$, additional defects are introduced, but much of the lattice remains intact. At $\lambda \geq 4$, the lattice structure is disrupted, and the high-potential particles exhibit larger neighbor distances than the low-potential particles. As in monodisperse systems, the loss of peak-splitting for $3 < \lambda < 4$ occurs near the visual loss of order. However, there are significant fluctuations in the bidisperse systems. While peak-splitting does not occur for $\lambda = 4$, box-spanning crystals occur at some time intervals during the simulation (not shown). The peak-splitting criterion represents a time-averaged structure.

The two autocorrelation functions and the cross-correlation function provide additional quantitative information about the system (Figure 9b). At $\lambda = 2$, the three correlation functions are almost identical, and all three exhibit peak-splitting in the second shell. As λ increases, the individual $g(r)$ measures move further out of phase. At $\lambda = 3$, the primary peaks become distinct as the A particles create more space around themselves relative to B particles. The second peaks reveal some splitting, with g_{AB} and g_{BB} dominating the first part of the split-peak and g_{AA} showing a stronger presence in the second part. For $\lambda \geq 4$, each individual $g(r)$ shows structuring in the second peak, but because they are all out of phase, the composite $g(r)$ in Figure 8a is smooth.

Because the runs in Figure 8b are at lower particle potentials than those in Figure 8a, they are closer to the order/disorder boundary of the monodisperse system (Figure 19a in ref 4). Surface structures [†structures and pair distribution functions described but not shown in this section are available in ref 26.] are similar to those of Figure 9a, except that coverages are higher and, accordingly, particle spacings are shorter. The lower particle potentials allow more particles to adsorb on the surface before the kinetically frustrated steady state is reached. For $\lambda \leq 1.67$, peak-splitting occurs, and a regular, substitutionally disordered lattice forms. For $2 \leq \lambda \leq 3$, local hexagonal structures still prevail, but the differing distances between different types of particles destroy the translational order sufficiently that the second $g(r)$ peaks do not split. At larger bidispersities, the global order is broken, although some particles that are surrounded by like particles still retain local 6-fold symmetry. The pair distribution functions (not shown) are similar to those of the previous case, except that the individual peak-splitting is not nearly as sharp. Even though surface coverage is higher, the weaker particle repulsions create a weaker ordered structure.

(26) Gray, J. J. Ph.D. Thesis, The University of Texas at Austin, Austin, TX, 2000.

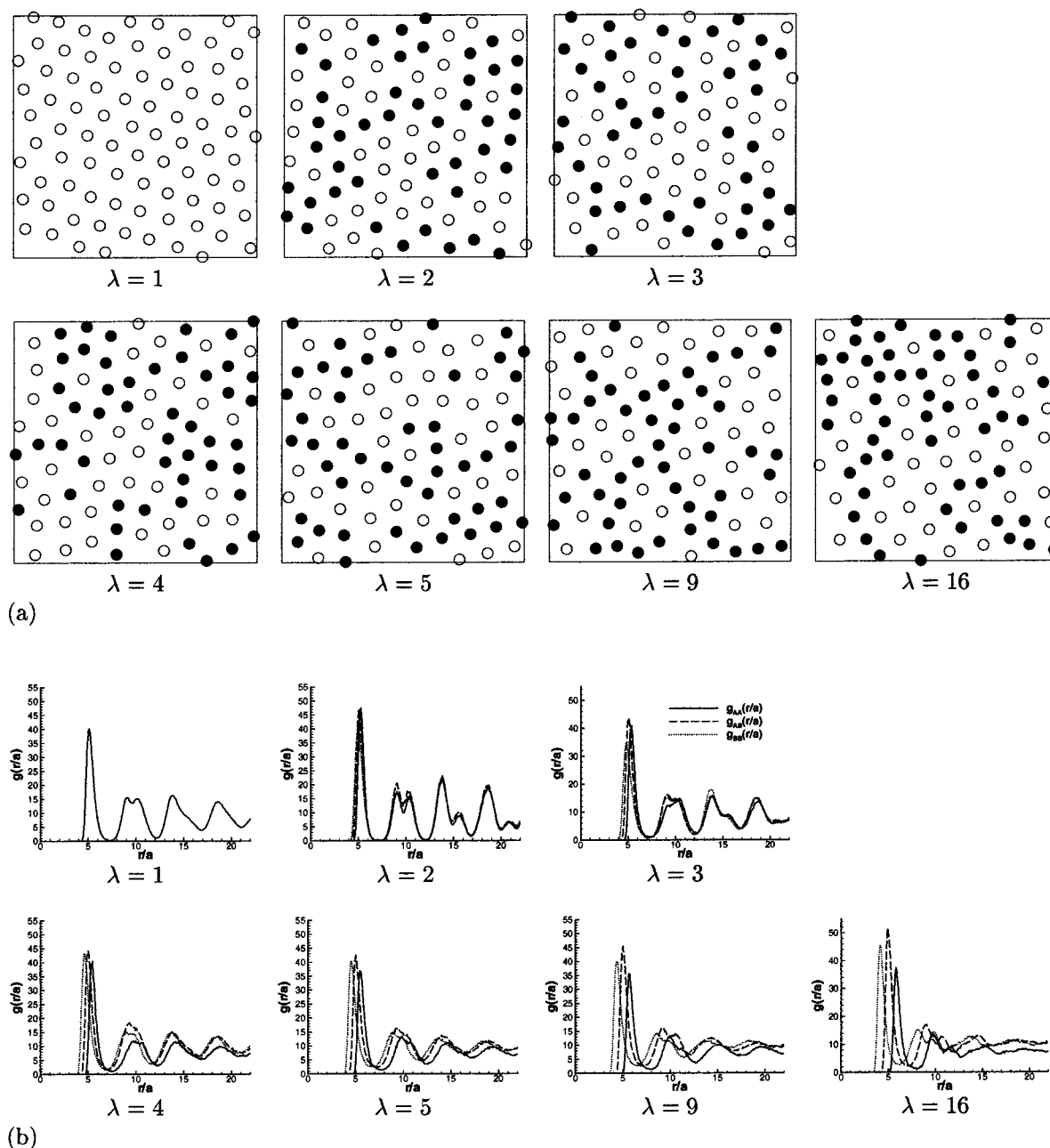


Figure 9. Breakup of order as bidispersity increases: (a) surface configurations and (b) pair distribution functions. $\kappa = 3$, $\Psi_w = -100$, and $\bar{\Psi} = 200$, corresponding to the total pair distribution plots in Figure 8a. Legend is the same as in Figure 6b.

Figure 10 shows total pair distribution functions for systems with longer range particle interactions ($\kappa = 1$), a mean particle potential of $\bar{\Psi} = 22.4$, and two different wall potentials. For $\Psi_w = -20$, which is slightly above the order/disorder boundary (near $-15 \leq \Psi_w \leq -10$, Figure 19b in ref 4), peak-splitting occurs for $\lambda \leq 1.25$ and does not occur for $\lambda \geq 1.5$, although a shoulder (but no minimum) is visible for $\lambda = 1.5$. The higher magnitude wall potential of $\Psi_w = -40$ creates greater stability: the peak-splitting boundary occurs within $1.75 \leq \lambda \leq 2$.

Figure 11 shows structures and auto- and cross-correlation functions corresponding to the runs in Figure 10b. At low bidispersities, a substitutionally disordered lattice forms, and the pair distribution functions have sharp peaks. At $\lambda = 1.75$, a cluster of B particles gathers, and the differing distances between different types of particles begin to smear the second broad peak in the pair distribution functions. At $\lambda = 2$, individual clusters retain local hexagonal symmetry, but the global clustering,

combined with different distances between neighbors of different types, breaks up the global order. For $\Psi_w = -20$ (not shown), systems obtain lower coverages, and the lower packing density destabilizes the substitutionally disordered phase: lines of particles twist at $\lambda = 1.25$ and break at $\lambda = 1.5$. Clusters of A and B particles form at $\lambda = 1.75$ and 4, and at $\lambda = 5$, B particles arrange into short lines between red particles. The peaks in the pair distribution functions for $\Psi_w = -20$ (not shown) are less sharp than at $\Psi_w = -40$, reflecting the lower stability of the lattice at lower magnitude wall potential.

Colloidal systems have been approximated as hard spheres by simply calculating an equivalent radius corresponding to an appropriate cutoff in the potential of eq 2.³¹ In ref 4, we showed that equivalent hard disk (EHD)

(27) Bocquet, L.; Hansen, J.-P.; Biben, T.; Madden, P. *J. Phys.: Condens. Matter* **1992**, *4*, 2375–2387.

(28) Vermöhlen, W.; Ito, N. *Phys. Rev. E: Stat. Phys., Plasmas, Fluids, Relat. Interdiscip. Top.* **1995**, *51*, 4325–4334.

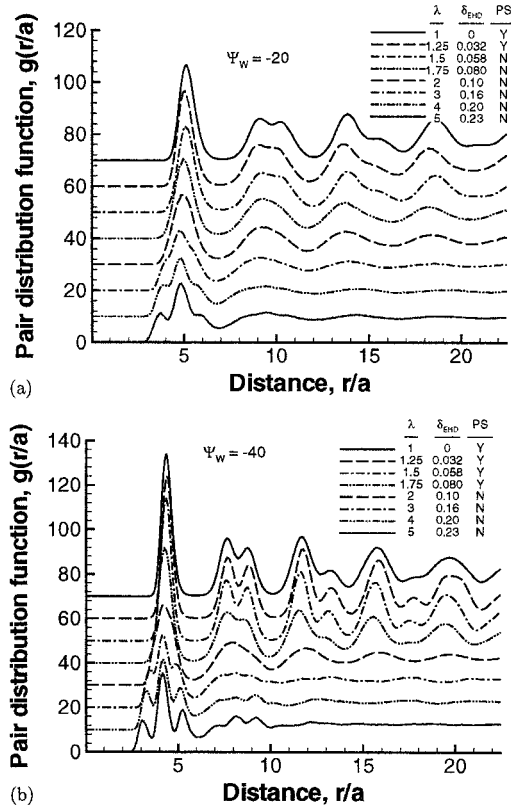


Figure 10. Pair distribution functions of adsorbed particles, showing the breakup of order as bidispersity is introduced for $\kappa = 1$, $\Psi = 22.4$, and $\phi_A = \phi_B = 0.005$. (a) $\Psi_w = -20$, and (b) $\Psi_w = -40$. Legend is the same as in Figure 8.

approximations provide rough estimates of coverages for $\kappa = 3$ systems but not for $\kappa = 1$ systems. In the bidisperse system, the EHD model maps the charge bidispersity to an equivalent size bidispersity. The EHD bidispersity ($\lambda_{\text{EHD}} = a_{\text{eff}}^A/a_{\text{eff}}^B$), where a_{eff}^A and a_{eff}^B is calculated from

$$a_{\text{eff}}^{(i)} = \frac{1}{2\kappa} \ln \frac{\alpha^{(i)}}{\ln \frac{\alpha^{(i)}}{\ln \dots}} \approx \frac{1}{2\kappa} \ln(\alpha^{(i)} / \ln \alpha^{(i)}) \quad (11)$$

with

$$\alpha^{(i)} = \xi \kappa \Psi_i^2 e^{2\kappa} \quad (12)$$

where $1/\xi$ is a cutoff potential set to unity for the current calculations. The EHD bidispersity, λ_{EHD} , is much smaller than the charge bidispersity, λ . For example, at the conditions of Figure 8a, $\lambda = 16$ corresponds to $\lambda_{\text{EHD}} = 1.43$. The fractional standard deviation of the particle size, $\delta_{\text{EHD}} = (a_{\text{eff}}^A - a_{\text{eff}}^B)/(a_{\text{eff}}^A + a_{\text{eff}}^B)$ is given in Figures 8–10.

When rescaled by effective hard disk size, ordered structures for the four sets of simulations of Figures 8 and 10 break up between $0.036 \leq \delta_{\text{EHD}} \leq 0.10$, depending on the conditions. In the $\kappa = 3$ case, peak-splitting is limited to $\delta_{\text{EHD}} \leq 0.036$ for $\bar{\Psi} = 100$ but extends to $\delta_{\text{EHD}} \leq 0.070$ for $\bar{\Psi} = 200$. In the $\kappa = 1$ case, peak-splitting ends at 0.058

$\leq \delta_{\text{EHD}} \leq 0.080$ for the low magnitude wall potential of $\Psi_w = -20$ and $0.080 \leq \delta_{\text{EHD}} \leq 0.10$ for the higher magnitude wall potential of $\Psi_w = -40$, reflecting the greater stability of the ordered phase at higher wall potentials. All of the terminal values of δ_{EHD} are equal to or less than that observed in other studies of both hard and soft disks, where estimates range from 0.06 to 0.10.^{27–30} The low terminal dispersities in the current system are possible because parameters such as wall potential can be manipulated to move the system closer to the monodisperse order/disorder phase boundary.

Sequential Adsorption. To this point, we examined the adsorption from a mixture of types of particles in a suspension. Here, we explore sequential adsorption of two types of particles; that is, the substrate is exposed to a suspension of one type of particle and then the partially covered surface is exposed to a second suspension with a different type of particle. We are again interested in accessible surface morphologies and, in particular, in determining whether the second exposure could change the state of the adsorbed system from ordered to disordered or vice-versa.

Table 1 summarizes the runs performed and the final surface coverages and morphologies, and Figures 12–17 depict surface configurations after the first and second exposure for selected runs. In the first set of runs, lower potential (B, black) particles are adsorbed first and higher potential (A, white) particles are adsorbed second. For the $\kappa = 1$ case, several A particles adsorb during the second exposure (Figure 12). In run 1, the A particles form isolated islands surrounded by B particles, similar to the first structure in Figure 4. In run 2, more A particles adsorb due to the higher magnitude wall potential and the shorter time of exposure to the first suspension. (At the conditions of the first exposure of run 2, the simulation becomes unstable at long times due to crowding on the surface leading to particle overlap. For this run, the first exposure was stopped early, before the surface saturated. All other first exposures in the sequential runs were continued to near completion or at least 95% of the extrapolated monodisperse jamming coverage.) In contrast to run 1, the snapshot for run 2 shows some formation of doublets and triplets of A particles.

In all cases in the first set of runs at $\kappa = 3$, no adsorption occurred during the second stage of the process. As described in ref 4, creation of a monolayer is a kinetically limited process: in these electrostatically stabilized systems, particle–particle repulsions prevent adsorption well before the thermodynamic limit. In the first set of runs with $\kappa = 3$, the short range of the wall interaction potential does not penetrate past the tightly packed repulsive monolayer, and further adsorption is prevented, whereas at $\kappa = 1$ the long-ranged attraction of the wall is sufficient for a particle to be drawn to the surface and to push other particles aside to create an adsorption site.

Figure 13 shows other surface structures created through the manipulation of the surface potential for the $\kappa = 1$ case. Run 5 is a modification of run 1 with an increased magnitude wall potential of $\Psi_w = -50$ during the second exposure. Additional A particles are drawn to the surface, increasing θ_2 dramatically from 0.009 to 0.064. A particles now form chains of multiple particles, in addition to isolated dots and pairs. The network of B particles is packed more tightly together than the original run 1.

In run 6, the first exposure is performed at conditions for which a regular lattice forms on the surface ($\Psi_w = -20$, and $\Psi_1 = 22.4$). During the second exposure, the magnitude of the wall potential is increased ($\Psi_w = -60$)

(29) Sadr-Lahijany, M. R.; Ray, P.; Stanley, H. E. *Phys. Rev. Lett.* **1997**, *79*, 3206–3209.

(30) Gray, J. J.; Klein, D. H.; Korgel, B. A.; Bonneau, R. T. *Langmuir* **2001**, *17* (8), 2317–2328.

(31) Russel, W. B.; Saville, D. A.; Schowalter, W. R. *Colloidal Dispersions*; Cambridge Monographs on Mechanics and Applied Mathematics; Cambridge University Press: Cambridge, U.K., 1989.

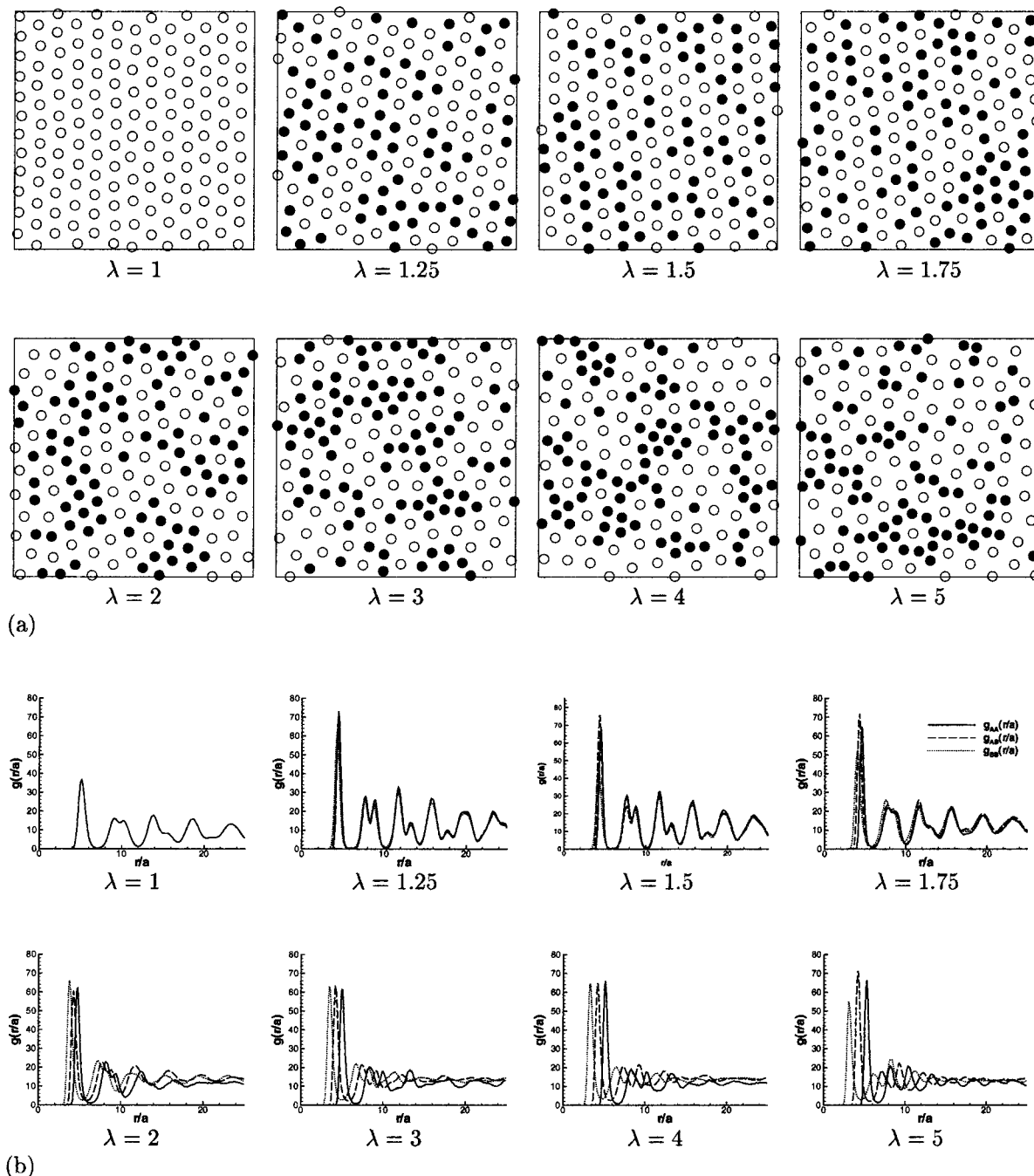


Figure 11. Breakup of order as bidispersity increases: (a) surface configurations and (b) pair distribution functions. $\kappa = 1$, $\Psi_w = -40$, and $\Psi = 22.4$, corresponding to the total pair distribution plots in Figure 10b. Legend is the same as in Figure 6b.

to drive additional adsorption up to $\theta_2 = 0.064$, approximately half of the surface coverage of the first species ($\theta_1 = 0.134$). The second exposure disrupts the global order sufficiently to remove the peak-splitting from the total pair correlation function (not shown). Lines of particles of each individual species can be drawn; the B particle network percolates through the particle box, but the A particle network is broken into lines and clusters that are slightly smaller than the box size.

In the third set of sequential runs, the higher potential species (A, white) is adsorbed first, and the lower potential species (B, black) is adsorbed second. In contrast to the first set of runs, the $\kappa = 1$ runs here do not show any adsorption during the second exposure, and the $\kappa = 3$ runs do show adsorption. Because of the longer range of the particle-particle repulsions in the $\kappa = 1$ case, B particles feel significant repulsions, even as they approach

interstices on the surface and are unable to adsorb. Figure 14 shows the configurations after both exposures for the $\kappa = 3$ case. In both cases, the first exposure establishes an ordered lattice of A particles. The second exposure adds B particles, which introduce some irregularity into the lattice, while the global order remains intact and the total pair correlation functions continue to exhibit peak-splitting. The lower particle potentials of run 10 ($\Psi_1 = 400$, and $\Psi_2 = 25$) allow more B particles to adsorb relative to that in run 9 ($\Psi_1 = 800$, and $\Psi_2 = 50$).

The fourth and fifth sets of sequential runs explore the variation in the potentials of the particles in the first and second exposures, using run 10 as a basis for comparison. As Ψ_1 decreases (Figure 15), the number of B particles that can adsorb decreases due to the tighter lattices at lower particle potentials. When A particle potentials are higher, particles are further apart, allowing larger inter-

Table 1. Sequential Adsorption Runs^a

	run	κ	first exposure					second exposure						
			Ψ_W or Ψ_{W1}	Ψ_1	t_1	θ_1	state	Ψ_{W2}	Ψ_2	λ	t_2	θ_2	θ_2^∞	state
set 1	1	1	-20	10	770	0.227	disorder		50	5	1000	0.009	0.010	disorder
	2	1	-40	10	200	0.265	disorder		50	5	570	0.035	0.036	disorder
	3	3	-100	50	3000	0.188	order		800	16	3000	0	0	order
	4	3	-100	25	3000	0.239	disorder		400	16	3000	0	0	disorder
set 2	5	1	-20	10	770	0.227	disorder	-50	50	5	210	0.064	0.066	disorder
	6	1	-20	22.4	1200	0.134	order	-60	50	2.2	1000	0.064	0.065	disorder
set 3	7	1	-20	50	870	0.091	order		10	1/5	500	0	0	order
	8	1	-40	50	810	0.113	order		10	1/5	500	0	0	order
	9	3	-100	800	3000	0.095	order		50	1/16	3000	0.003	0.022	order
	10	3	-100	400	3000	0.105	order		25	1/16	3000	0.019	0.027	order
set 4	11	3	-100	200	2000	0.130	order		25	1/8	3000	0.014	0.021	order
	12	3	-100	100	3000	0.157	order		25	1/4	3000	0.006	0.009	order
set 5	13	3	-100	400	3000	0.105	order		50	1/8	3000	0.014	0.019	order
	14	3	-100	400	3000	0.105	order		100	1/4	3000	0.006	0.010	order
set 6	15	3	-100	400	3000	0.105	order	-200	25	1/16	3000	0.033	0.076	order
	16	3	-100	400	3000	0.105	order	-400	25	1/16	3000	0.054	0.094	order

^a Ψ_1 and Ψ_2 are the particle potentials from the first and second suspension; Ψ_{W1} and Ψ_{W2} are the wall potentials during the first and second exposures if they differ; t_1 and t_2 are the adsorption exposure times; θ_1 and θ_2 are the surface coverage fractions at the end of the exposures; and θ_2^∞ is the jamming limit predicted by extrapolating coverage of the second species with a 2/3-power law.²⁵ $\lambda = \Psi_2/\Psi_1$. Ordered and disordered states indicate the presence of peak-splitting in the second shell of neighbors of the total pair distribution function.

Set 1: $\kappa = 1$, $\Psi_1 = 10$, $\Psi_2 = 50$

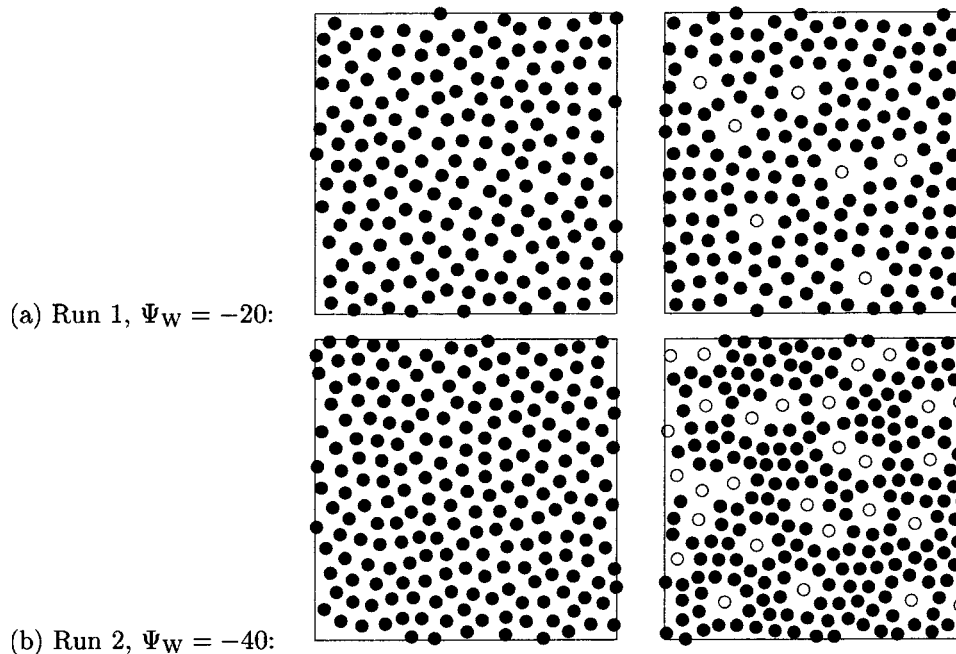


Figure 12. High-potential particles (A, white) adsorbed after low-potential particles (B, black) for two different wall potentials. (a) Run 1 and (b) run 2; left and right snapshots show the final state after the first and second exposures, respectively. The first exposure of run 2 was not allowed to achieve steady state. See Table 1 for complete conditions.

stices through which B particles can reach the surface. However, the addition of B particles in run 12 does not disrupt the lattice as it does in run 11. As Ψ_2 increases (Figure 16), the number of B particles that adsorb decreases. Because particle–particle repulsions kinetically frustrate the colloidal adsorption process, higher potential particles are more repelled by particles already adsorbed on the surface and thus adsorb less.

The patterns in sets 3–5, which consist of a regular lattice of A particles with a small percentage of B particles added, might be useful as “doped superlattices”. Doped two-dimensional photonic crystals would have altered optical properties, and doped arrays of quantum dots would have altered electrical properties.

Figure 17 shows that the amount of doping in a superlattice can be controlled with the wall potential

during the second exposure. As observed for the $\kappa = 1$ case of set 2 (Figure 13), increasing the wall potential drives additional particle adsorption. In this case, θ_2 increases from 0.019 in run 10 to 0.054. The B particles adsorb in several clusters, and the cluster size increases as the wall potential is increased.

Lattice Models and Equivalent Hard Disks

There are no models for predicting the structure of adsorbed monolayers of particles. However, lattice models and models based on EHDs both provide useful reference points. Broadly speaking, lattice models assume a global structure and then calculate energies to place particles inside the structure, whereas EHD models assume a constant energy to calculate sizes and infer global structure.

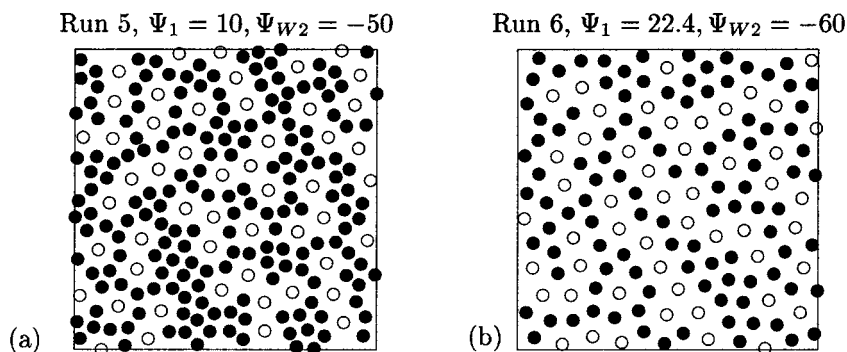
Set 2: $\kappa = 1, \Psi_{W1} = -20, \Psi_2 = 50$ 

Figure 13. High-potential particles adsorbed after low-potential particles with increased wall potential during the second exposure. (a) Run 5 and (b) run 6. See Table 1 for conditions.

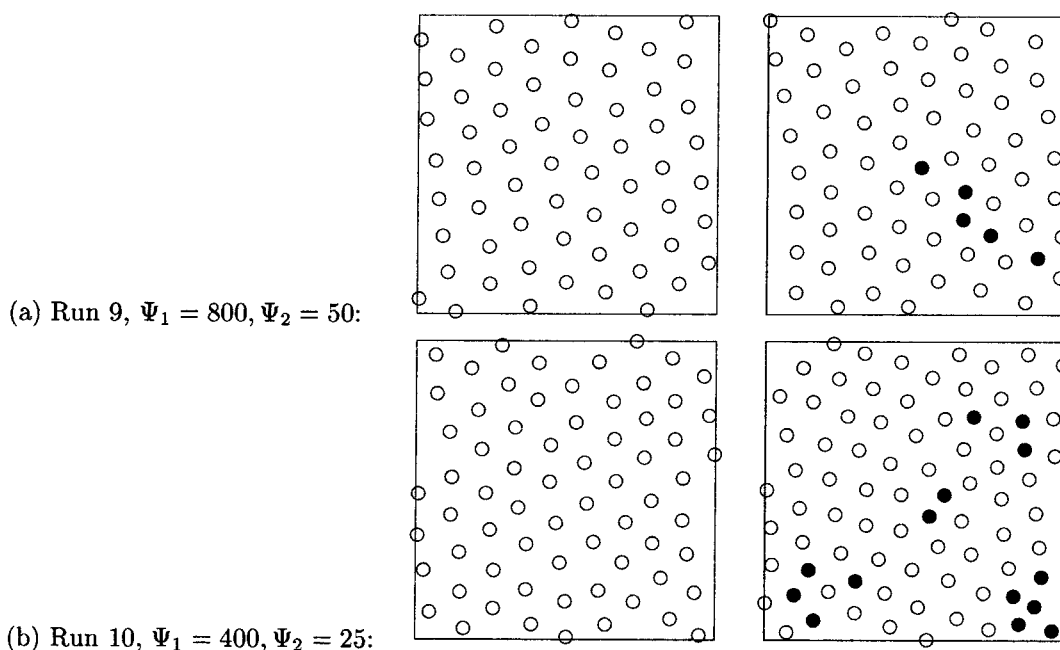
Set 3: $\kappa = 3, \Psi_W = -100$ 

Figure 14. Low-potential particles (B, black) adsorbed after high-potential particles (A, white) for two different mean particle potentials. (a) Run 9 and (b) run 10. See Table 1 for conditions.

Lattice models compare to the present simulations only when the monolayer orders. The systems studied here are characterized by very strong attractions between the particles and the substrate. Therefore, in the ordered configuration, almost all “lattice sites” are occupied by a particle, and the structure of the lattice can be mapped onto the $s = 1/2$ Ising model on a triangular lattice.⁸ Particles experience significant repulsions, with the mixed interaction potential (V_{AB}) having a strength near the geometric mean of the like-component interaction potentials (V_{AA} and V_{BB}). In an equilibrium lattice system, these parameters would create a phase of pure A (the more highly charged component with the strongest interaction with the substrate). At lower wall potentials (unfortunately, lower than the monodisperse order/disorder boundary), an A_2B phase would prevail, and at still lower wall potentials, an AB_2 phase would exist.⁸ None of these morphologies manifest themselves in the simulations in this study.

The simulations show that colloidal adsorption differs from lattice model predictions primarily because it does not achieve equilibrium. Particles that adsorb are strongly

attached to the wall and do not desorb: a B particle will not be replaced by an A particle, even though the latter is energetically favored on the surface. Second, repulsions between particles prevent adsorption beyond a certain limit, even though energetics favor additional adsorption.⁴

Although there is no exchange of particles between the bulk and the surface, we can infer structure through ground-state energy calculations, given the fixed composition of an ordered bidisperse monolayer. In a lattice, all nearest-neighbor distances η are equal, and the energetic cost for breaking like pairs of neighbors in exchange for two unlike pair bonds is

$$2V_{AB} - V_{AA} - V_{BB} = (2\Psi_A\Psi_B - \Psi_A^2 - \Psi_B^2)f(\eta) \\ = -(\Psi_A - \Psi_B)^2 f(\eta) < 0 \quad (13)$$

where $f(\eta) = e^{-\kappa(r_1-2)/\eta}$. Because the interchange energy is always negative, mixed pairs of neighbors are always favored energetically in screened electrostatic systems on lattices. The preference for AB neighbors over AA or BB pairs increases with the disparity in particle potentials.

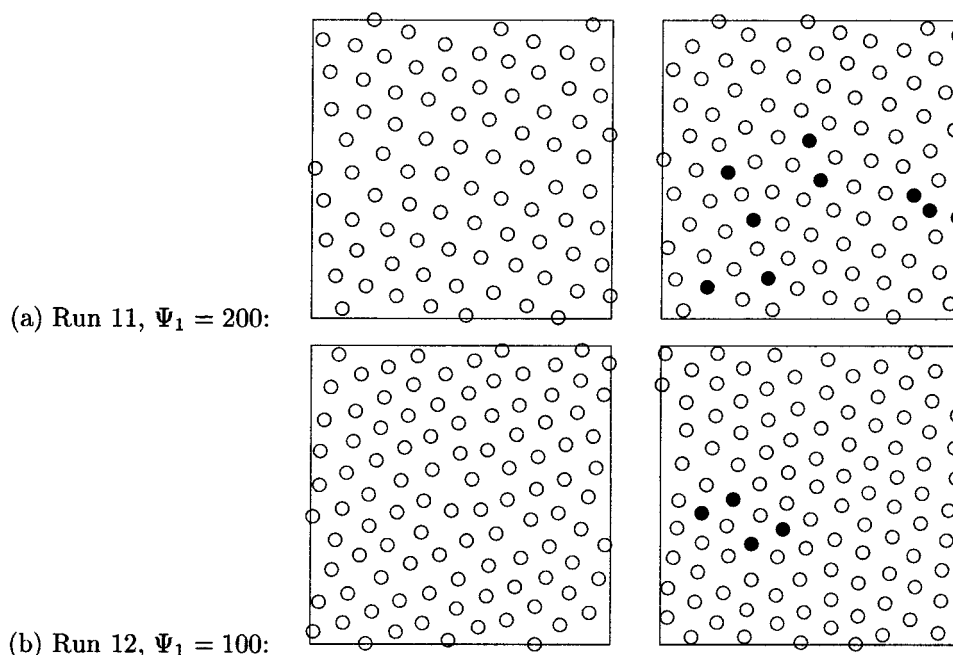
Set 4: $\kappa = 3, \Psi_W = -100, \Psi_2 = 25$ 

Figure 15. Low-potential particles adsorbed after high-potential particles for different values of the high-particle potential, Ψ_1 . (a) Run 11 and (b) run 12, cf. also Run 10 in Figure 14. See Table 1 for conditions.

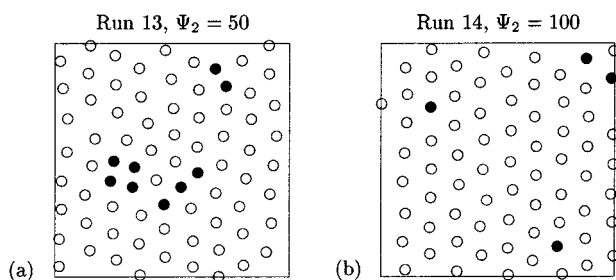
Set 5: $\kappa = 3, \Psi_W = -100, \Psi_1 = 400$ 

Figure 16. Low-potential particles adsorbed after high-potential particles for different values of the high-particle potential, Ψ_1 . (a) Run 13 and (b) run 14, cf. also Run 10 in Figure 14. See Table 1 for conditions.

Thus, A_2B and AB_2 structures are energetically favored for monolayers with the correct composition. There are two reasons that these structures do not occur in simulated systems. First, although disordered monolayers exhibit rapid surface diffusion and restructuring, particles on the lattice do not rearrange easily, and the structure of ordered monolayers is often effectively fixed after formation. Thus, the monolayer structure is kinetically frustrated from finding its lowest energy state.

Second, lattice models are inaccurate because simulations show that the distances between neighbors vary according to the particle type, increasingly straining the lattice assumption as bidispersity increases. A second type of model, the EHD model, predicts the distance between neighbors and has been used to predict phase behavior for suspensions of colloidal particles.³¹ This model assumes a constant interparticle potential, and the distances between neighbors vary to achieve a constant potential between all pairs in the system. Consequently, the interchange energy of eq 13 is zero, and all neighbors are equivalent.

If the present system behaved as EHDs, complete phase separation would be predicted (in the low-temperature

Table 2. Interparticle Distances Predicted by EHD Theory (r_{EHD}) and Observed in Simulation (r_{sim} , Defined as the Location of the Primary Peak in the Measured Pair Correlation Function)^a

pair	a			pair	b		
	r_{EHD}	r_{sim}	$V(r_{\text{sim}})$		r_{EHD}	r_{sim}	$V(r_{\text{sim}})$
AA	5.48	5.25	18.5	AA	5.41	5.36	1.27
AB	4.15	4.15	14.0	AB	4.55	4.55	1.06
BB	2.90	3.05	11.5	BB	3.69	3.74	0.92

^a $V(r_{\text{sim}})$ is the interparticle potential calculated at r_{sim} . (a) $\kappa = 1$, $\Psi_A = 50$, $\Psi_B = 10$, $\Psi_W = -40$, and the cutoff potential for EHD calculations is 14.0. (b) $\kappa = 3$, $\Psi_A = 400$, $\Psi_B = 25$, $\Psi_W = -100$, and the cutoff potential for EHD calculations is 1.06. The mixed pair (AB) r_{EHD} is determined by replacing Ψ_i^2 with $\Psi_A \Psi_B$ in eq 12. To obtain the accuracy shown, the calculations of r_{EHD} include several terms in the expansion of eq 11.

limit) because maximum packing favors phase separation between large and small particles for radius ratios greater than 0.637.¹¹ Although local demixing is seen in disordered cases and in some sequential adsorption runs, complete phase separation does not occur (although this may be because of simulation size). The distances between particles in simulation differ from that expected from EHD theory. In general, the A particles are closer than expected, thus experiencing higher pair potentials, and the B particles are further apart, experiencing lower pair potentials (Table 2). EHD radii match better for short-range interaction potentials ($\kappa = 3$).

In summary, lattice models predict intimately mixed structures such as the AB_2 phase, and EHD models predict phase separation, while simulations produce an intermediate array of structures including chains and clusters of particles. Colloidal mixtures behave in a fashion intermediate between the EHD model and the lattice models, and further work is necessary to develop a complete theory to describe system morphology. Such a theory would include not only the interparticle energetics but also the entropy of mixing, the number of particles of each type on the surface, the placement of particles as

Set 6: $\kappa = 3$, $\Psi_{W1} = -100$, $\Psi_1 = 400$, $\Psi_2 = 25$

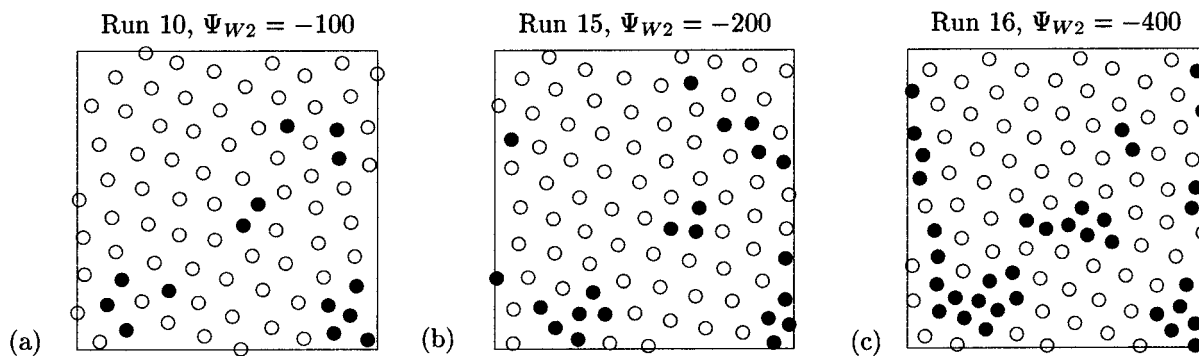


Figure 17. Effect of wall potential during the second exposure: low-potential particles adsorbed after high-potential particles. (a) Run 10, (b) run 15, and (c) run 16. See Table 1 for conditions.

they are added to the surface, and the thermal energy present in the system to allow rearrangement. The morphologies observed here are not equilibrium structures, and they depend on the manner in which they are produced. At the moment, simulation remains the best tool to capture this behavior and explore the effects of parameter variations.

Conclusions

To pursue the formation of complex adsorbed microstructures, we extended our efficient, parallel simulations of the adsorption of colloidal particles to bidisperse mixtures. Competitive adsorption strongly influences coverage behavior, and templating processes may be useful for designing specific surface features. The ζ -potential ratio necessary to disrupt order ranges from 1.5 to 3, depending on the salt concentration, wall potential, and mean particle potential. Sequential adsorption processes

can be used to create mixed phases with small fractions of a second component, but exposure parameters must be selected carefully to ensure that adsorption is not kinetically frustrated by repulsions of preadsorbed particles. Increasing wall potential magnitude during the second exposure induces additional adsorption. Lattice models and EHD calculations provide useful reference points for comparison, but neither capture the system behavior due to the nonequilibrium nature of the process.

Acknowledgment. We gratefully acknowledge the National Science Foundation (Grant CTS-9358409), the Packard Foundation for a fellowship for R.T.B., the W. M. Keck Foundation and the University of Texas Thrust 2000 Program for a graduate fellowship for J.J.G., and the Texas Advanced Computing Center for computational resources.

LA0012844